Available online at www.sciencedirect.com
ScienceDirect
Thermochimica Acta 463 (2007) 32–40
thermochimica acta
www.elsevier.com/locate/tca

The melting behavior of aluminum nanoparticles

J. Sun [a], S.L. Simon [a,b,*]

[a] *Department of Chemical Engineering, Texas Tech University, Lubbock, TX 79409, USA*
[b] *Laboratoire de Chimie Physique, Université Paris Sud, F-91405 Orsay, France*

Available online 17 July 2007

Abstract

The melting behavior of aluminum nanoparticles having an oxide passivation layer is examined using a differential scanning calorimetry (DSC). Both broad and narrow size-distributed particles are studied, and the weight-average particle radius ranges from 8 to 50 nm. With decreasing particle size, the melting response moves towards lower temperatures and the heat of fusion decreases. The effect of the oxide coating on the particles is to apply a compressive force to the aluminum core, thereby increasing the observed melting point and the heat of fusion. The melting point depression, both corrected and uncorrected for the effects of the oxide shell, is linear with the reciprocal of particle radius, as predicted by Gibbs–Thomson equation, although only the corrected data give a value of the solid–liquid interfacial tension comparable to those reported in the literature. The size-dependent heat of fusion is significantly smaller than that predicted by the effects of the surface tension indicating that the solid nanoparticle is at a higher energy than expected, presumably due to the presence of defects or irregularities in the crystal structure at or emanating from the surface. This hypothesis is tested using our data, as well as using data in the literature for tin nanoparticles.

Keywords: Aluminum nanoparticles; Melting; Heat of fusion; Melting temperature; Defects

1. Introduction

The properties of nanoparticles, including the melting point depression and the size-dependent heat of fusion, have been of interest to researchers for the last 60 years [1–16]. Small particles have lower melting points than bulk material due to an increased proportion of surface atoms as the size of particles decreases. The size-dependent melting point depression of nanoparticles has been experimentally observed using various techniques, such as scanning electron-diffraction, field emission, transmission electron microscopy, X-ray diffraction, calorimetry, and other techniques [2–14]. Many metals have been studied, including gold [2–4], silver [3], tin [5–7], indium [8–10], lead [11,12], and aluminum [14,15]. For gold nanoparticles obtained by the condensation of vapor gold on a carbon substrate, a 500 K depression has been reported for particles of 1 nm-radius using the scanning electron-diffraction technique [2] The melting behavior of several organic materials and indium metal, at nanometer length scales, has also been studied using calorimetry by confining the material in controlled porous glasses [16,17].

The melting point depression for small crystals can be described in a classical thermodynamic approach by the so-called Gibbs–Thomson equation [18–21]. The result for spherical particles is

$$T_m(r) = T_m(\infty) - \frac{2T_m(\infty)\sigma_{sl}}{\Delta H_f(\infty)\rho_s r} \quad (1)$$

where $T_m(\infty)$, $\Delta H_f(\infty)$, and ρ_s are the bulk melting temperature, the bulk latent heat of fusion, and the solid phase density, respectively. r represents the radius of a spherical particle and $T_m(r)$ is the melting point of a particle with radius r. σ_{sl} is the solid–liquid interfacial energy. The Gibbs–Thomson equation, which predicts a linear relationship between the melting point depression and the inverse of particle size, has been used to describe the behavior of low molecular weight organic liquids in confined geometry [16], to describe the melting point depression of cadmium embedded in an aluminum matrix [13], and to explain the melting temperatures of polymer lamella crystals [21,22]. The equation can be obtained following an analogous derivation to that of Defay and Prigogine for the boiling point depression by capillary condensation [19]; the derivation

* Corresponding author.
E-mail address: sindee.simon@ttu.edu (S.L. Simon).

0040-6031/$ – see front matter © 2007 Elsevier B.V. All rights reserved.
doi:10.1016/j.tca.2007.07.007

is based on the equality of the chemical potentials of the two phases and the use of the Laplace formula to describe the relationship between the pressure and the surface tension. For the liquid–vapor transition examined by Defay and Prigogine [19], it is assumed that the specific volume and thermal expansion coefficient of the vapor phase are much larger than those of the liquid; such assumptions are not necessarily valid for the solid–liquid transition. If these assumptions are not invoked, the size-dependent melting point depression is given by the following:

$$\left(\frac{T_m(r)}{T_m(\infty)}\right)^C = 1 - C\frac{2\sigma_{sl}}{\Delta H_f(\infty)\rho_s r} \quad (2)$$

where the constant $C = T_m(\rho_s/(\rho_s - \rho_l))(\alpha_{ls} - \alpha_s)$, ρ_s and ρ_l are the densities of the solid and liquid, respectively, and α_l and α_s are the thermal expansion coefficients of the two phases. An expansion of the left hand side to two terms results in the form of Eq. (1); however, this approximation is not expected to be valid for large depressions or for values of C much greater than 1. We note that for the solid–liquid transition of aluminum nanoparticles investigated in this work, $C = 1.04$.

Other models for the dependence of the melting point on crystal size exist [2,3,6–12,14,24–27]. Most predict essentially the same relationship as the Gibbs–Thomson equation (that T_m varies with the reciprocal size) except that the surface tension of the liquid in contact with solid (σ_{sl}) in the Gibbs–Thomson equation is replaced by α which has been shown to differ slightly among the models [10,11]. For example, in the liquid-skin model, $\alpha = \sigma_{sl}/((1 - t_o)/r) + \sigma_{lv}((1 - \rho_s)/\rho_l)$, where t_o is the thickness of the liquid skin surrounding the solid particle [10]. Since our particles are coated with an oxide passivation layer, such a model is not expected to be pertinent.

Although the depression of the melting point at the nanoscale has been examined by many researchers, fewer calorimetric measurements have been made investigating the size-dependent heat of fusion. In the derivation of the Gibbs–Thompson equation, it is assumed that the heat of fusion decreases with particle size due to the increase in the surface energy [19]:

$$\Delta H_f(r) = \Delta H_f(\infty) - \frac{2\sigma_{sl}}{\rho_s r} \quad (3)$$

where $\Delta H_f(r)$ represents the heat of fusion for a particle with radius r, and the derivation of Eq. (3) is based on the equilibrium melting process and the Laplace formula [19]; for the solid–liquid transition, the correction factor C discussed above should be multiplied by the surface tension term. However, this equation is found to severely underestimate the depression in the heat of fusion (whether or not the factor C is used), as will also be shown in this work for our passivated aluminum particles. It is noted that the liquid skin model, which predicts that the heat of fusion should be proportional to the cube root of the reciprocal particle radius, is able to reasonably predict the depressions in the melting point and the heat of fusion for tin [6,7] but for other materials, including indium [10] and aluminum [15] nanoparticles and for organic compounds confined in controlled porous glass [16], it does not seem to give a good description.

At small enough size scales, materials often fail to crystallize and, instead, undergo a glass transition [28]. It has also been postulated that a critical point may exist at the nanoscale where the solid and liquid phases show identical properties and where the heat of fusion would, therefore, become zero. Koga and coworkers, using molecular dynamics simulations, found evidence of a solid–liquid critical point for ice confined to carbon nanotubes [29] Although a solid–liquid critical point cannot occur in bulk materials, other evidence for such a critical point at small size scales includes the absence of the calorimetric signatures for melting or for the glass transition for *cis*-decaline and cyclohexane confined to 2 nm pores [16].

In this work, we investigate the melting behavior of aluminum nanoparticles. Such particles are of interest due to the variety of their applications, including propellants, munitions, pyrotechnics, additives for plastics, and powder metallurgy. These nanoparticles have an aluminum oxide passivation layer on the order of several nanometers thick which increases stability and reduces agglomeration. Limited work has been done by other researchers on the melting behavior of aluminum at the nanoscale [14,15]. Lai et al. investigated the melting point depression of aluminum nanoclusters using a nanocalorimetric technique [14]. The aluminum nanoclusters were obtained through vapor-deposition of aluminum onto a Si_3N_4 surface, and in situ nanocalorimetry measurements were conducted immediately after the deposition; therefore, the aluminum nanoparticles do not have an oxide layer. Lai et al. found that the melting point of these aluminum clusters is significantly reduced compared to the bulk value and the data could be well described by the liquid skin model; these researchers did not report heat of fusion data [14]. Eckert et al. studied the melting behavior of aluminum powders generated using mechanical attrition [15]. Depending on the atmosphere used in the mechanical attrition process (argon, oxygen, or hydrogen), different surface layers were formed. Both the melting point and heat of fusion of the aluminum nanopowders studied by Eckert et al. decreased with decreasing particle size. However, the thickness of the surface layer was not well quantified; the results also indicated that the nature of the surface layer had no significant effect on the melting behavior.

In the work reported here, we use differential scanning calorimetry (DSC) to study the melting behavior of aluminum nanoparticles that are generated through a gas condensation process and have a well-characterized oxide layer several nanometers thick. We first describe our materials and experimental methods, including DSC and thermogravimetric analysis (TGA), the latter of which yields the aluminum content of the passivated particles. We then present our results, followed by discussion and a conclusion.

2. Methodology

2.1. Materials

Five aluminum nanoparticle samples were used in this work. The aluminum nanoparticles were obtained from Technanogy

Table 1
Physical properties of aluminum nanoparticle samples

Particle radius[a] (nm)	Weight-average radius (nm)	Active Al content (%)		Oxide layer thickness (nm)	
		Supplier	Our measurement	Supplier	Our measurement
12.5 ± 10.50	26.7 ± 8.7	54	47.5	1.8	5.3
21.5 ± 0.95	21.6 ± 1.0	74	56.5	1.5	3.4
31.5 ± 1.55	31.7 ± 1.6	82	68.5	1.4	3.3
40.5 ± 1.50	40.7 ± 1.5	84	71.4	1.6	3.8
46.0 ± 1.25	46.1 ± 1.3	83	72.3	1.9	4.2

[a] Mean radius ± Standard Deviation.

(Irvine, CA), and the physical properties of these nanoparticles are listed in Table 1. The sample with an average size of 12.5 nm radius has a broad size distribution with a standard deviation of 10.5 nm. The other four samples have narrow size distributions with standard deviations of less than 2 nm. Also used in the study were micron-size aluminum particles (3–4.5 μm, 97.5% purity); these were purchased from Alfa Aesar (Milwaukee, WI). The average particle diameter and standard deviation of the nanoparticles were obtained from SEM images by Pantoya and coworkers, and a typical size distribution curve has been published [30]. Other characteristics, including surface area and size distribution, of the nanopowders have been reported; [31] similar data is available for the micron-size particles [32].

Since the average particle size obtained from SEM experiments reflects the number size distribution, whereas the heat flow response in DSC experiments corresponds to the weight distribution of the sample, the number-average particle size is converted to weight-average size assuming that the particles have Gaussian distribution; the weight-average sizes are shown in Table 1. We note that although the log normal distribution has been used to describe the particle size distribution for particles generated using the same technique [33,34], the Gaussian distribution has been shown to describe the particle size distribution well for vapor-deposited indium nanoparticles [35], and the calculated active aluminum content of our particles is closer to the experimental values when we assume a Gaussian distribution than when we assume a log normal distribution [23]. Other researchers have also assumed a Gaussian distribution in their work to mathematically demonstrate the influence of size distribution on the oxidation wave speed [36]

As already discussed, each aluminum nanoparticle is passivated with a 3–5 nm Al_2O_3 layer. As the particle size decreases the total percentage of Al_2O_3 increases and can become a considerable amount of the total powder. In Table 1, the aluminum content (Al content) refers to the amount of aluminum present, i.e., that aluminum which is not in the form of Al_2O_3. The aluminum content was obtained from mass gain measurements using TGA as described in a subsequent section. Although our measurements showed a lower aluminum content compared to measurements made by the supplier, the aluminum content changes less than 3% during storage in our laboratory based on the results of TGA experiments conducted two months apart. Based on our measurement of the aluminum content, the size of the aluminum core and the thickness of the oxide layer (t_{oxide}) can be calculated through a mass balance [23]:

$$t_{oxide} = R_o \left[1 - \left(\frac{\rho_{Al_2O_3} c}{\rho_{Al} + c(\rho_{Al_2O_3} - \rho_{Al})} \right)^{1/3} \right] \quad (4)$$

where R_o is the total particle size (including the oxide layer), c is the fractional aluminum content, and $\rho_{Al_2O_3}$ (3.05 g cm^{-3}) [37] and ρ_{Al} (2.7 g cm^{-3}) [38] are the densities of amorphous aluminum oxide and aluminum at room temperature, respectively. The oxide layer is assumed to be amorphous based on the results of other researchers [32]; if the layer is assumed to be crystalline, its thickness is on average 43% thinner than that reported in Table 1.

Since the aim of this work is to examine the effect of aluminum particle size on the melting point depression and on the heat of fusion, we were interested in studying particles smaller than those available from the manufacturer. To that end, the aluminum nanoparticles with the average particle mean size of 21.6 nm were selectively oxidized in either a Perkin-Elmer TGA-7 or DSC-7 at 500 °C under 25/75 O_2/Ar atmosphere for various times ranging from 30 min to 20 h in order to make the active aluminum core smaller. Based on the mass gained during oxidation and the aluminum content of the partially oxidized particles, the aluminum core radius after oxidation was calculated assuming no change in the size distribution of the particles. The active aluminum core size ranges from 18 nm down to 8 nm after oxidation and the amorphous oxide layer is correspondingly thicker, ranging from 4 to 16 nm. The reproducibility of aluminum core radius obtained from TGA and DSC oxidization processes are ±0.3 and ±0.6 nm, respectively, based on three experiments conducted with the same oxidation time.

2.2. Differential scanning calorimetry (DSC)

The melting behavior of the aluminum nanoparticles was studied using a Perkin-Elmer Pyris 1 DSC with an ethylene glycol/water cooling system to maintain a stable DSC head temperature and to avoid frost build-up on the instrument. All the experiments were performed under an argon atmosphere. Both gold and alumina DSC pans were used in the experiment. The gold pans were used to examine the nanoparticles' melting behavior due to the higher thermal conductivity of gold. However, the gold pan could only be used for aluminum nanoparticles having an oxide layer since the oxide layer prevents alloy formation of gold and aluminum; hence, the micron-sized aluminum

particles and bulk aluminum foil were run in the alumina pans. The mass of the DSC samples varied from 1.00 to 3.50 mg. A scan rate of 5 K/min was used. The obtained heat flow responses were corrected using baseline subtraction. The extrapolated peak onset temperature was used to define the melting point because compared with the peak temperature, the extrapolated onset temperature is less dependent on heating rate, sample thermal conductivity, sample mass, and sample thickness [39,40]. The heat of fusion (J/g sample) was obtained by the integration of heat flow over the DSC melting peak, and the heat of fusion per gram of aluminum was calculated based on the aluminum content in the sample as determined from our TGA measurements (see below). Since the heat of fusion is obtained from the integrated heat flow, it is not affected by any smearing of the transition resulting from heat transfer effects. In addition, we note that some nanoaluminum samples were run in both gold and alumina pans; the values of the heat of fusion obtained were the same within the error of the measurements indicating that heat transfer effects do not effect ΔH_f measurements. The reproducibility of DSC experiments based on repeat experiments of three samples are better than $\pm 0.5\,^{\circ}C$ for the melting point and $\pm 5\%$ for the heat of fusion.

The temperature of the instrument was calibrated using zinc, potassium sulfate, and potassium chromate at a heating rate of 5 K/min under argon atmosphere for both types of pans. The heat flow was calibrated using potassium sulfate.

2.3. Thermogravimetric analyzer (TGA)

Although the aluminum nanoparticles were stored under argon atmosphere after delivery, they may have reacted with adventitious oxygen between the time that the supplier made the measurements of aluminum content and our DSC experiments. Therefore, the aluminum content was determined using a Perkin-Elmer TGA-7. The temperature of the instrument was calibrated using nickel and iron at a heating rate of 5 K/min. The mass of the TGA samples varied from 1 to 3 mg and a 25/75 mixture of O_2/Ar was used as the analysis gas. All the samples were held for 960 min at 830 °C in order to completely oxidize the aluminum particles. The mass gain in TGA is attributed to oxidation of aluminum, and the aluminum content (c) can, thus, be calculated using the following equation based on a mass balance and the mass ratio of aluminum to oxygen in Al_2O_3 [23]:

$$c(\%) = \frac{108}{96}\Delta m(\%) \quad (5)$$

where $\Delta m(\%)$ is the mass gain in the TGA experiment. As already noted, the aluminum content changes less than 3% during the storage in our laboratory based on the results of TGA experiments conducted two months apart.

3. Results

Typical DSC melting responses are shown in Fig. 1 for three aluminum nanoparticle samples. The DSC curves were obtained upon heating at 5 K/min under argon atmosphere. The heat flow is normalized by the mass of aluminum, which was calculated from the total sample mass and aluminum content obtained from TGA. Fig. 1 shows that with decreasing particle size, the melting response moves to lower temperatures, and the heat of fusion, which is obtained from the integrated peak area, decreases with decreasing particle size. Repeat scans on a single DSC specimen give the same melting peak with changes in T_m of less than 1 K and changes in ΔH_f of less than 10%, confirming that the oxide layer protects the aluminum core such that no significant agglomeration occurs between the particles during the DSC scan. The results of repeat scans also indicates that there is little reaction of adventitious or adsorbed oxygen with the nanoparticles during the scan.

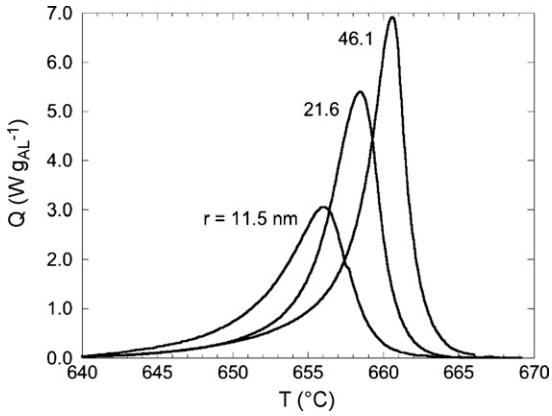

Fig. 1. Melting response for three representative narrow size distribution aluminum nanoparticles at 5 K/min under argon atmosphere; heat flows are normalized by mass of aluminum in the core of the nanoparticle, as determined from TGA. The radius indicated is the weight-average radius.

The melting point of the aluminum nanoparticles is plotted as a function of weight-average core radius in Fig. 2 for all samples studied; the melting point is obtained from the onset of the melting peak for reasons discussed in the experimental section. With decreasing particle size, the melting point decreases with a depression of 4 K observed for aluminum nanoparticles of 46 nm radius and 13 K for aluminum nanoparticles of 11 nm. The solid

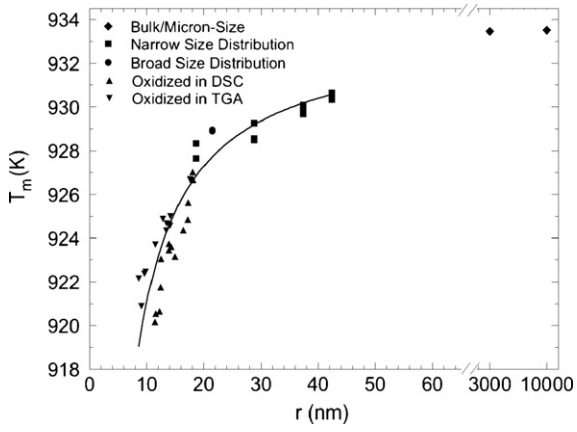

Fig. 2. Melting point depression as a function of the weight-average aluminum core radius r. The solid lines in the figure are the fits to the Gibbs–Thomson equation. The symbols represent the bulk sample, narrow size distribution samples (as received), the broad size distribution sample (as received), and the narrow size distribution samples after selective oxidation in the DSC or TGA.

line in the figure represents the best fit for the Gibbs–Thomson equation. Both the broad and narrow size-distributed particles, and the partially oxidized particles are in good agreement with the equation. Note that if we used the number-average radius of 12.5 nm for the broad distribution sample instead of weight-average size of 26.7 nm, the sample would show a significant deviation form the rest of the data confirming the importance of using a weight-average size. The melting points of aluminum nanoparticles partially oxidized in DSC 7 appear to be lower than those oxidized in TGA 7 presumably due to differences in oxidization in these two instruments: based on the appearance of the samples oxidized in the TGA and DSC, the aluminum nanoparticles are more uniformly oxidized in DSC, i.e., the color is more uniform for the same extent of oxidization. The size distribution of the final sample is assumed to be the same as in the initial narrow size distribution. Although this is expected to be the case if oxidation is uniform, if it is not, e.g., in the TGA, a broader distribution will result which should shift the weight-average radius to higher values; since we assume that the size distribution does not change with oxidation, the TGA-oxidized samples appear to have higher melting points than their DSC counterparts.

Although the Gibbs–Thompson equation fits the data shown in Fig. 2, the fit gives a low value for the solid–liquid surface tension: $\sigma_{sl} = 68 \pm 2\,mJ/m^2$ for $T_m(\infty) = 933.52\,K$ [35], $\Delta H_f = 396\,J/g$ [35], and $\rho_s\,(T_m) = 2.55\,g/cm$ [41]. The value is lower than those reported in the literature: a value of $93\,mJ/m^2$ was reported using nucleation experiments [42]; a value of $163\,mJ/m^2$ was found by grain boundary groove measurements [43]; and a value of $149\,mJ/m^2$ was obtained from molecular dynamic simulation [44]. We show later that the disagreement is due to the presence of the oxide layer which results in a compressive pressure on the aluminum core, thereby reducing the magnitude of the melting point depression (i.e., elevating the melting point above what would be measured without the pressure effect).

The data shown in Fig. 2 are replotted in Fig. 3 as a function the reciprocal of particle size along with a comparison between our data and that of Lai et al. [14] and Eckert et al. [15] Our data show a much smaller melting point depression than either of other two, in part due to the effect of the compressive effect of oxide layer (see later). However, the data of Lai et al. and of Eckert et al. also differ significantly, presumably because of the differences in the shapes, structure, surface properties, and/or mechanical stresses of the nanoparticles due to different fabrication methods—Lai et al.'s particles were vapor deposited whereas Eckert's were mechanically milled. The solid lines represent the best fit for Gibbs–Thomson equation for each data set in the inset and the dashed lines show the fits to the liquid skin model. The data of Lai et al. follow Gibbs–Thomson reasonably well yielding a value $135 \pm 5\,mJ/m^2$ for σ_{sl}; the data also fit the liquid-skin model and Lai et al. obtained a value of $140\,mJ/m^2$ for σ_{sl} with a critical liquid shell thickness t_0 of 1.2 nm using a value of $\sigma_{lv} = 914\,mJ/m^2$. The data of Eckert et al. do not fit either model well, although the liquid skin model fits their smaller particle sizes. For our data, a value of $137 \pm 6\,mJ/m^2$ was obtained for σ_{sl} from the liquid skin model with a value of -0.7 ± 0.6 nm for the liquid shell thickness t_o. The fact that the liquid shell thickness is essentially zero for our data is perhaps not unexpected because we expect to not have a liquid layer due to the presence of the oxide layer (i.e., the atoms at the particle surface are expected less mobile if they are in contact with aluminum oxide as compared to surface atoms in contact with a gas).

The latent heat of fusion (per gram of aluminum in the particle core) obtained from our experimental work is shown in Fig. 4 as a function of the weight-average aluminum core radius. For all the nanosize samples studied, the heats of fusion obtained from DSC experiments are lower than that of the bulk material, decreasing from 88% of the bulk value for the 46 nm radius particles to approximately 20% for the smallest particles studied. The latent heat of fusion for aluminum foil and for 3 μn size particles equal the bulk value (396 J/g) within 1%. The heat of fusion data of Eckert et al. [15] is also shown in the figure. Both our data and that of Eckert et al. show a significant reduction of the heat of fusion with decreasing particle size, especially at smaller sizes, but their data shows a stronger depression at small sizes; the differences between our results and theirs are attributed to the

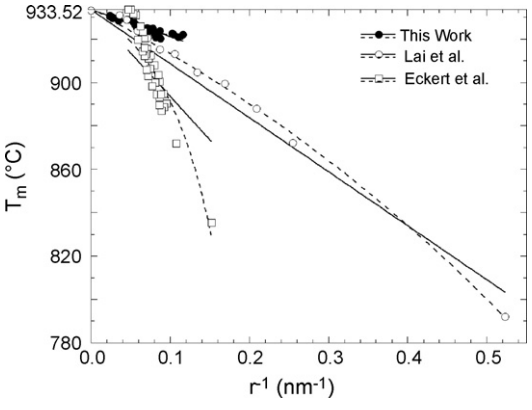

Fig. 3. Melting point depression versus reciprocal radius r, along with data from Lai et al. [14] and Eckert et al. [15]. The solid lines are the fits to the Gibbs–Thomson equation; the dashed lines are the fits to the liquid skin model.

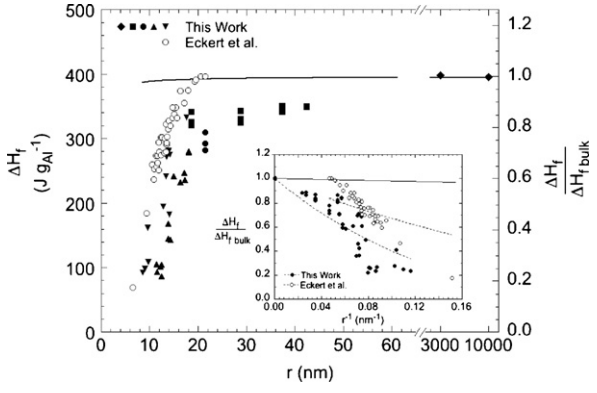

Fig. 4. Normalized heat of fusion as a function of weight-average aluminum core radius r; the y_2-axis shows the scale for the fractional heat of fusion. The symbols are the same as in Fig. 2. The data of Eckert et al. [15] is also indicated. The inset shows the two data sets plotted against the reciprocal radius. The solid line represents the best fit for Eq. (3) for all the data; the dashed lines show the fit of the liquid skin model.

difference in the particles due to different fabrication techniques. The solid line in Fig. 4 shows the size-dependent heat of fusion predicted from Eq. (3) (which corrects the heat of fusion for the surface energy) using the nominal value of 100 mJ/m^2 for σ_{sl}; the equation clearly does not describe either our data or the data of Eckert et al. without invoking values of σ_{sl} that are orders of magnitude larger than reported in the literature. In passing, we also note that the liquid skin model also does not describe the data of Eckert et al.

4. Discussion

4.1. Effect of oxide layer

As mentioned previously, the aluminum nanoparticles studied have an aluminum oxide layer, which may contribute to the differences between our results and those of other researchers. The confinement of the aluminum core by the oxide layer is expected to result in the core experiencing a compressive pressure due to the differential thermal expansion between the aluminum and aluminum oxide. The change in the melting point due to the compressive pressure applied by the shell to the aluminum core can be calculated using the integrated form of the Clausius–Clapeyron equation [45] assuming small temperature changes:

$$\Delta T_m = T_m(P) - T_m(1\,\text{bar}) = (P - 1\,\text{bar})\frac{T_m(\infty)}{\Delta H_f(\infty)}\left(\frac{1}{\rho_l} - \frac{1}{\rho_s}\right) \quad (6)$$

where P is the pressure and ΔT_m is the change of melting temperature due to the pressure effect. The pressure is that induced by the differential thermal expansion between the aluminum core and the aluminum oxide shell; some of this pressure may be relieved by the compliance of the oxide shell:

$$P = K\{(\alpha_{Al} - \alpha_{Al_2O_3})(T_m(\infty) - T_r) - [(\varepsilon + 1)^3 - 1]\} + 1\,\text{bar} \quad (7)$$

where K is the bulk modulus of aluminum ($=E/(3-6\nu)$ with E being the Young's modulus and ν being the Poisson's ratio), $\alpha_{Al_2O_3}$ and α_{Al} are the coefficients of thermal expansion for Al_2O_3 and Al, respectively, $T_m(\infty)$ is the bulk melting point of aluminum, ρ_l and ρ_s represent the liquid and solid density of aluminum, and ε is the strain of the oxide shell. Eq. (7) is derived from the definition of the bulk modulus coupled with the assumption that the volumetric strain is due to a term involving differential thermal expansion minus a term related to the volumetric strain in the aluminum core due to compliance of the oxide shell. The magnitude of the pressure also depends on the temperature at which the oxide layer is formed (i.e., the stress-free temperature T_r). Complicating the issue is the fact that the oxide layer, which is originally amorphous, crystallizes between 300 and 635 °C during a DSC temperature scan [46]. Hence, we take T_r to be near the end of point of crystallization; we show later that the value of the surface tension σ_{sl} depends on the value of T_r.

Table 2
Material properties for $\Delta T_m(P)$ calculations

Constant	Value	Description	Reference
K	75 GPa	Bulk modulus of Al	[40]
$\alpha_{Al_2O_3}$	24×10^{-6} K^{-1}	Coefficient of thermal expansion of Al_2O_3	[40]
α_{Al}	77×10^{-6} K^{-1}	Coefficient of thermal expansion of Al	[43]
ρ_l	2.38 g/cm^3	Liquid density of Al	[42]
ρ_s	2.55 g/cm^3	Solid density of amorphous Al	[35]
Y	500 GPa	Biaxial modulus of Al_2O_3	[42]

The pressure P in Eq. (7) will depend on particle size and shell thickness since the biaxial stress σ and biaxial strain ε in the oxide shell depend on particle size and shell thickness [47]:

$$\sigma = \frac{(P - 1\,\text{bar})}{4}\frac{b^3 + 5a^3}{b^3 - a^3} = Y\varepsilon \quad (8)$$

where a and b are the radius of aluminum core and entire particle, respectively, and Y is the biaxial modulus of the oxide ($=E/(1-\nu)$). The material properties used to calculate the effect of the oxide shell on the melting point are given in Table 2. Note that since the oxide layer is crystalline at temperatures above T_r during the DSC scan, the values of $\alpha_{Al_2O_3}$ is that for crystalline aluminum oxide.

The melting points corrected to 1 bar (assuming $T_r = 615$ °C) using Eqs. (6)–(8) are plotted in Fig. 5 as a function of weight-average radius and the results are compared with the measurements of Lai et al. [14]. The good agreement indicates that much of the difference observed in Fig. 2 was indeed due to the pressure effects induced by the oxide layer. For a particle with $a = 42.5$ nm and $b = 46.7$ nm, a compressive pressure of 52 MPa is obtained, resulting in an increase in T_m of 6.5 K above that which would be measured at 1 bar. For smaller particles with thicker oxide shells, higher pressures are obtained: for $a = 8.6$ nm and $b = 24.3$ nm, the compressive pressure is 119 MPa, resulting in an increase in T_m above that at 1 bar of 19.2 K. The solid line represents the best fit for Gibbs–Thomson equation

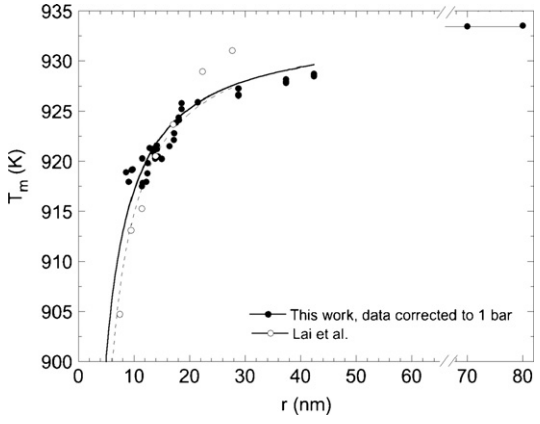

Fig. 5. Comparison of our melting point data corrected to $P = 1$ bar for the melting point depression of aluminum with the data of Lai et al. [14]. The solid line represents the best fits for Gibbs–Thomson equation for our data. The dashed line represents the best fit for the liquid skin model for Lai et al.'s data.

and gives a value of 101 mJ/m^2 for σ_{sl}, also in good agreement with literature values. Obviously, the value of σ_{sl} obtained will depend upon the assumed value of the stress-free temperature, T_r: σ_{sl} varies from 177 mJ/m^2 for $T_r = 550\,^\circ$C to 78 mJ/m^2 for $T_r = 635\,^\circ$C. Values of T_r in this range are reasonable given the temperature range in which the amorphous oxide crystallizes; these values of σ_{sl} also span the range of values reported in the literature.

We note that our calculations of the pressure in the oxide-coated aluminum particle are considerably lower than that of 88,000 atm recently arrived at by other researchers [48]. Although the details of their calculation are not specified, we suggest that this unrealistically high pressure may be due to assuming that the relevant volume change is that due to melting. We argue that the expansion on melting is not relevant to our calculation because the onset of melting (which is what is measured in the DSC) is dictated by the pressure of the system at the incipient point of melting and is thereby unaffected by the volume change that occurs during the process. The wide breadth of the melting peaks, on the other hand, could be due to an increase in pressure as the material melts due to the associated volume expansion. However, pressures expected based on a 10% volume change and neglecting shell compliance are on the order of 8 GPa; such pressures would give unrealistically high values of T_m (using the Clausius–Clapeyron equation) and are inconsistent with the melting behavior observed.

The compressive pressure on the aluminum core due to the differential thermal expansion between the aluminum and aluminum oxide will also increase the value of heat of fusion measured:

$$\Delta(\Delta H_f) = \Delta H_f(P) - \Delta H_f(1\,\text{bar}) = \frac{1}{\rho_s}[1 - (\alpha_{Al} - \alpha_{Al_2O_3})(T_m(\infty) - T_r)](P - 1\,\text{bar}) \quad (9)$$

The compressive pressure results in an increase in the heat of fusion over what would be measured at 1 bar. For example, for the sample with $a = 42.5$ nm and $b = 46.7$ nm, an increase in ΔH_f of 20.7 J/g (5% of the bulk) is calculated, and for a sample with $a = 8.6$ nm and $b = 24.3$ nm the increase is 46 J/g (12% of the bulk value). The modified heats of fusion for all the samples are shown in Fig. 6. The solid line gives the expected result based on Eq. (3) using $\sigma_{sl} = 101$ mJ/m^2. Obviously, the correction for ΔH_f goes in the opposite direction and does not reconcile the lack of agreement between the data and Eq. (3).

4.2. Origin of depression of ΔH_f

The depression of the heat of fusion is considerably larger than that expected based on Eq. (3). The limited data in the literature on the heat of fusion depression for nanoparticles and for materials confined to the nanometer length scale [16,17] show similar results. For example, the heat of fusion of heptane in a 4 nm diameter nanopore [16] is approximately 30% of the bulk value, whereas it is expected to be closer to 90% based on the σ_{sl} calculated from melting point depression; and for indium metal

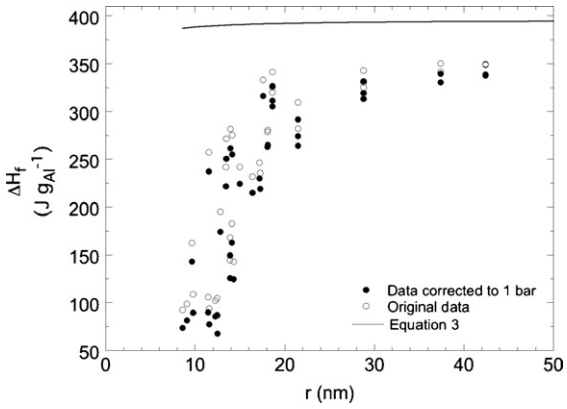

Fig. 6. Comparison of the original heat of fusion data with those corrected to $P = 1$ bar as a function of aluminum core radius r. The solid line represent the value obtained from Eq. (3) using a value of σ_{sl} of 101 mJ/m^2.

confined in porous glasses [17], the measured heat of fusion in an 8.2 nm nanopore is 15 J/g compared to 27 J/g predicted from Eq. (3) using the σ_{sl} obtained from the melting point depression.

The postulated explanation for the large depressions in the heat of fusion observed in nanoscopic systems is an increasing fraction of lattice defects or irregularities in the crystal structure with decreasing particle size at the nanoscale. We suggest that the experimental heat of fusion of our aluminum nanoparticles can be expressed in the following form:

$$\Delta H_f(r) = \Delta H_f(\infty) - \frac{2\sigma_{sl}}{\rho_s r} - \Delta H_{defect}(r) \quad (10)$$

where the first two terms are the size-dependent heat of fusion using the σ_{sl} obtained from the melting point depression, and $\Delta H_{defect}(r)$ is the enthalpy depression due to the defects, which is hypothesized to be size dependent. From Eq. (10), $\Delta H_{defect}(r)$ can be calculated using the value of σ_{sl} obtained earlier (101 mJ/m^2). The results are shown in Fig. 7 as a function of weight average particle radius. The number of defects in the nanoparticles (per gram of the aluminum core) can be directly related to the enthalpy of defects if one assumes that

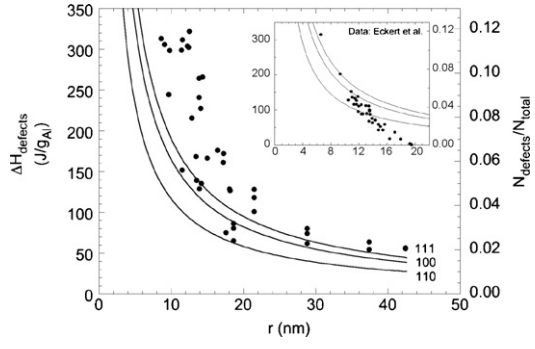

Fig. 7. ΔH_{defect} as a function of the weight-average aluminum core radius r. The y_2-axis indicates the fraction of lattice defects relative to the total number of atoms in the aluminum core assuming $\Delta H_{defects}$ is due to lattice defects. The curves show the fraction of surface atoms at the interface relative to the total number of atoms in the core for the three fcc crystal planes indicated. The inset shows the data of Eckert et al. [15] treated in the same manner; the x- and y-axes have the same units for the inset as in the main figure although the x-axis scale is reduced in the inset.

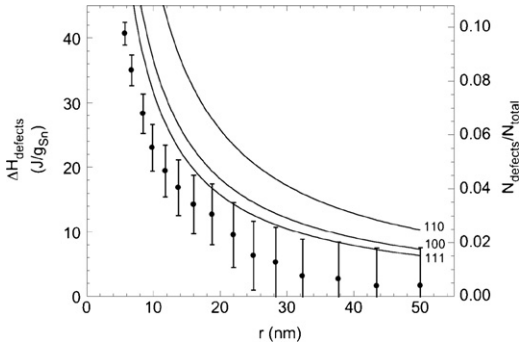

Fig. 8. ΔH_{defect} as a function of the particle radius r for tin nanoparticles based on the enthalpy of fusion data reported by Lai et al. [6]. Error bars on the data points are based on error bars reported for ΔH_f in Ref. [6]. The y_2-axis indicates the fraction of lattice defects relative to the total number of atoms in the nanoparticle assuming $\Delta H_{defects}$ is due to lattice defects. The curves show the fraction of surface atoms relative to the total number of atoms in the particle for the three body-centered tetragonal crystal planes indicated.

the defects are lattice point defects, which for aluminum have an energy of 73.3 kJ/mol defects [49]. The right-hand y-axis in Fig. 7 shows the scale for the fraction of defects (number of defects per number of total aluminum atoms in the core) calculated from $N_{defects}/N_{total} = 0.000368\ \Delta H_{defect}(r)$ for $\Delta H_{defect}(r)$ in J/g_{Al}, where the constant is simply the molecular weight of aluminum divided by the defect energy in J/mol. Also plotted in Fig. 7 is the fraction of aluminum atoms at the interface between the aluminum core and the aluminum oxide relative to the total number of atoms in the nanoparticle; three curves are shown representing the aluminum surface to volume ratios as a function of particle size for the 1 0 0, 1 1 0, and 1 1 1 face-centered cubic crystal planes. These curves are calculated from $N_{surface}/N_{total} = (3/4)fa/r$, where in this formula, a is the aluminum lattice constant of 0.405 nm [50], r is the particle radius, and f is a factor that equals 2 for the 1 0 0 plane, $2^{1/2}$ for the 1 1 0 plane, and $4/3^{1/2}$ for the 1 1 1 plane. Interestingly, the fraction of defects appears to be very closely related to the fraction of atoms at the aluminum/aluminum oxide interface suggesting that defects at the interface or propagating from the interface may be responsible for the decrease in the enthalpy of melting at the nanoscale.

The inset of Fig. 7 shows the milled aluminum nanoparticle data of Eckert et al. [15] treated in the same manner; in this case, the fraction of defects is several times smaller than the fraction of surface atoms except at the smallest particle sizes. As already discussed, the differences between the two systems presumably arise because Eckert's particles were mechanically milled, although it should be noted that if mechanical milling resulted in plastic deformation, one might expect more, rather than fewer, vacancy defects [49].

To further test the generality of our hypothesis that the decrease in the enthalpy of fusion at the nanoscale may be related to defects in the solid crystal structure at or emanating from the surface, we apply the same analysis to the heat of fusion of thermally evaporated tin nanoparticles reported by Lai et al. [6]. Fig. 8 shows the enthalpy of defects calculated from Eq. (10) for Lai et al.'s tin nanoparticles taking the bulk enthalpy of fusion as 60.6 J/g [37], the solid density as 7.31 g/cm^3 [37], and the solid–liquid surface tension as 48 mJ/m^2 [6]. Also shown in the same figure on the right-hand y-axis is the fraction of defects in the nanoparticles given the vacancy defect energy of 49.2 kJ/mol defects for tin [49]. In order to examine whether the number of defects are related to the atoms at the surface, three curves are plotted, showing the fraction of surface atoms in the particles as a function of particle size for the densest 1 0 0, 1 1 0, and 1 1 1 planes in the body-centered tetragonal β-tin crystal; for the 1 0 0 and 1 1 0 planes, the curves are calculated from $N_{surface}/N_{total} = (3/2)fa/r$, where a is the tin lattice constant of 0.583 nm [51] and f is a factor that equals 1 for the 1 0 0 plane and $2^{1/2}$ for the 1 1 0 plane; for the 1 1 1 plane, $N_{surface}/N_{total} = (3/2^{1/2})ac/[r(c^2 + a^2/2)^{1/2}]$, where c is the tin lattice constant of 0.318 nm. Similar to our data for aluminum nanoparticles, a correlation between the number of defects and the number of surface atoms is found. In addition, the heat of fusion appears that it will become zero in both the tin system studied by Lai et al. and in our passivated aluminum particles when the percentage of defects is approximately 12–14%.

Our hypothesis is that the decrease in the enthalpy of fusion at the nanoscale arises from an increase in the energy of the solid due to the presence of defects in the crystal structure at or emanating from the surface/interface; consequently, the number of defects increases relative to the total number of atoms as the size scale decreases and the surface to volume ratio increases. This idea is conceptually similar to a model recently proposed by Delogu [52] in which the decrease in enthalpy is attributed to the particle in its "solid" state having a higher energy due to the presence of excited surface atoms with highly irregular structure, and it is similarly analogous to the liquid-layer model [10,11] where the higher energy of the "solid" phase is due to the presence of a mobile liquid layer of finite thickness. However, although we expect that our surface atoms have an irregular structure, we do not expect their mobility to be high (as in a liquid) because of their intimate contact with the aluminum oxide shell. On the other hand, the fact that the model also reasonable describes the behavior of tin nanoparticles having free surfaces indicates that the concept of defects or irregularities in structure at the surface/interface may provide a more general way to describe the dependence of enthalpy on size at the nanoscale in a variety of systems, including the passivated aluminum particles studied here, materials confined in nanoporous matrices, and particles that may have a more mobile free surface.

5. Summary

The melting behavior of aluminum nanoparticles having an aluminum oxide layer is examined using DSC. The weight-average aluminum core size studied ranges from 8 to 50 nm. With decreasing particle size, the melting response moves towards lower temperatures and the heat of fusion decreases. The oxide layer results in a compressive pressure on the aluminum core. After correcting for this pressure effect, a value of σ_{sl} of 101 mJ/m^2 was obtained by fitting the Gibbs–Thomson equation, in good agreement with values reported in the literature.

The depression in the heat of fusion is found to be considerably larger than that expected based on the surface tension. It is suggested that the decrease in the heat of fusion at the nanoscale is due to an increase in the energy of the solid due to the presence of defects or irregularities in the crystal structure. The fraction of defects in the nanoparticles is calculated from the heat of fusion assuming point defects and is found to correlate with the fraction of atoms at the interface/surface both for our passivated aluminum particles, as well as for tin particles studied by other researchers. This result suggests that the origin of the depression of the heat of fusion at the nanoscale is related to defects at or emanating from the surface (or interface) of the nanoparticle or nanoconfined material. Furthermore, the heat of fusion appears that it will become zero when the percentage of lattice defects is approximately 12–14%.

Acknowledgement

The authors gratefully acknowledge Professor G.B. McKenna for his suggestions and discussions. This work was supported by the National Science Foundation DMR 0304640.

References

[1] N. Ichinose, Y. Ozaki, S. Kashu, Superfine Particle Technol. (1992) 1–38.
[2] Ph. Buffat, J.-P. Borel, Phys. Rev. A 13 (1976) 2287.
[3] T. Castro, R. Reifenberger, Phys. Rev. B 42 (1990) 8548.
[4] K. Dick, T. Dhanasekaran, Z.Y. Zhang, D. Meisel, J. Am. Chem. Soc. 2312 (2002).
[5] C.R.M. Wronski, Brit, J. Appl. Phys. 18 (1967) 1731.
[6] S.L. Lai, J.Y. Guo, V. Petrova, G. Ramanath, L.H. Allen, Phys. Rev. Lett. 77 (1996) 99.
[7] T. Bachels, H. Güntherodt, Phys. Rev. Lett. 85 (2000) 1250.
[8] M. Dippel, A. Maier, V. Gimple, H. Wider, W.E. Evenson, R.L. Rasera, G. Schatz, Phys. Rev. Lett. 87 (2001) 095505.
[9] C.J. Coombes, J. Phys. Metal Phys. 2 (1972) 441.
[10] M. Zhang, M.Y. Efremov, F. Schiettekatte, E.A. Olson, A.T. Kwan, S.L. Lai, T. Wisleder, J.E. Greene, L.H. Allen, Phys. Rev. B 62 (2000) 10548.
[11] K.F. Peters, J.B. Cohen, Y. Chung, Phys. Rev. B 57 (1998) 13430.
[12] K.F. Peters, Y. Chung, J.B. Cohen, Appl. Phys. Lett. 71 (1997) 2391.
[13] D.L. Zhang, J.L. Hutchinson, B. Cantor, J. Mater. Sci. 29 (1994) 2147.
[14] S.L. Lai, J.R.A. Carlsson, L.H. Allen, Appl. Phys. Lett. 72 (1998) 1098.
[15] J. Eckert, J.Y. Holzer, C.C. Ahn, Z. Fu, W.L. Johnson, Nanostruct. Mater. 2 (1993) 407.
[16] C.L. Jackson, G.B. McKenna, J. Chem. Phys. 93 (1990) 9002.
[17] K.M. Unruh, T.E. Huber, C.A. Huber, Phys. Rev. B 48 (1993) 9021.
[18] J.W. Gibbs, The Collected Works of J. Willard Gibbs, Yale University Press, New Haven, 1948.
[19] R. Defay, I. Prigogine, Surface Tension and Adsorption, John Wiley and Sons, Inc, 1967.
[20] L. Makkonen, Langmuir 16 (2000) 7669.
[21] B. Wunderlich, Macromolecular Physics, vol. 3, Academic Press, 1980.
[22] J.E. Mark, Physical Properties of Polymers Handbook, AIP Press, 1996.
[23] J. Sun, Ph.D. Thesis, Texas Tech University, 2004.
[24] H. Reiss, I.B. Wilson, J. Colloid Sci. 3 (1948) 551.
[25] Z. Zhang, X.X. Lü, Q. Jiang, Physica B 270 (1999) 249.
[26] Z. Zhang, J.C. Li, Q. Jiang, J. Phys. D: Appl. Phys. 33 (2000) 2653.
[27] K.K. Nanda, S.N. Sahu, S.N. Behera, Phys. Rev. A 66 (2002) 013208.
[28] C. Alba-Simionesco, G. Dosseh, E. Dumont, B. Frick, B. Geil, D. Morineau, V. Teboul, Y. Xia, Eur. Phys. J. E 12 (1) (2003) 19.
[29] K. Koga, G.T. Gao, H. Tanaka, X.C. Zeng, Nature 412 (6849) (2001) 802.
[30] M. Pantoya, S. Son, W. Danen, B. Jorgensen, B. Asay, J. Busse, J. Mang, Characterization of metastable intermolecular composites (MICs), in: A.W. Miziolek, S.P. Karna, J.M. Mauro, R.A. Vaia (Eds.), Defense Applications of Nanomaterials, ACS Symposium Series 891, Copyright American Chemical Society, 2005, pp. 227–240 (Chapter 16).
[31] D. Pesiri, C.E. Aumann, L. Bilger, D. BOoth, R.D. Carpenter, R. Dye, E. O'Neil, D. Shelton, K.C. Walter, J. Pyrotechn. 19 (2004) 19–31.
[32] M.A. Trunov, M. Schoenitz, X. Zhu, E.L. Dreizin, Combust. Flame 140 (2005) 310–318.
[33] D.E.G. Jones, R. Turcotte, Q.S.M. Kwok, M. Vachon, L. Guindon, D. Lepage, V.Y. Gertsman, NATAS Proceedings, 2004.
[34] C.E. Aumann, G.L. Skofronick, J.A. Martin, J. Vacuum Sci. Technol. 13 (1995) 1178.29–1183.29;
J.J. Granier, M.L. Pantoya, Combust. Theory Model. 8 (2004) 555.
[35] M. Zhang, M.Y. Efremov, F. Schiettekatte, E.A. Olson, A.T. Kwan, S.L. Lai, T. Wisleder, J.E. Greene, L.H. Allen, Phys. Rev. B 62 (2000) 10548–10557.
[36] J.J. Granier, M.L. Pantoya, Combust. Theory Model. 8 (2004) 555–565.
[37] R.C. Weast, Handbook of Chemistry and Physics, CRC Press, 1973.
[38] I. Levin, D. Brandon, J. Am. Ceram. Soc. 18 (8) (1998) 1995–2012.
[39] G. Höhne, Differential Scanning Calorimetry: An Introduction for Practitioners, Springer Verlag, 2003.
[40] J. Schawe, C. Schick, Thermochim. Acta 187 (1991) 335–349.
[41] G. Simmons, H. Wang, Single Crystal Elastic Constant and Calculated Aggregate Properties: A Handbook, second ed., The MIT Press, 1971.
[42] D. Turnbull, J. Appl. Phys. 21 (1950) 1022.
[43] J.R. Morris, Phys. Rev. B 66 (2002) 144104.
[44] Z. Jian, K. Kuribayashi, W. Jie, Mater. Trans. 45 (2002) 721.
[45] J.M. Smith, H.C. Van Ness, M.M. Abbott, Introduction to Chemical Engineering Thermodynamics, fifth ed., Mc-Graw-Hill, New York, 1996.
[46] E.L. Dreizin, M.A. Trunov, M. Schoenitz, The 1st Workshop on Pyrotechnic Combustion Mechanisms, Fort Collins, USA, July 10, 2004.
[47] R.J. Roark, W.C. Young, Formulas for Stress and Strain, fifth ed., McGraw-Hill, New York, 1975.
[48] A. Rai, D. Lee, K. Park, M.R. Zachariah, J. Phys. Chem. B 108 (2004) 14793.
[49] I. Kovacs, H. El Sayed, J. Mater. Sci. 11 (1976) 529.
[50] W. Witt, Z. Naturforsch. A 22A (1967) 92.
[51] V.T. Deshpande, D.B. Sirdeshmukh, Acta Crystallogr. 14 (1961) 355.
[52] F. Delogu, J. Phys. Chem. 109 (2005) 21938.